SIAM J. SCI. COMPUT.
Vol. 25, No. 6, pp. 2066–2083

# SIMULATIONS OF THE WHIRLING INSTABILITY BY THE IMMERSED BOUNDARY METHOD*

SOOKKYUNG LIM† AND CHARLES S. PESKIN†

**Abstract.** When an elastic filament spins in a viscous incompressible fluid it may undergo a whirling instability, as studied asymptotically by Wolgemuth, Powers, and Goldstein [*Phys. Rev. Lett.*, 84 (2000), pp. 16–23]. We use the immersed boundary (IB) method to study the interaction between the elastic filament and the surrounding viscous fluid as governed by the incompressible Navier–Stokes equations. This allows the study of the whirling motion when the shape of the filament is very different from the unperturbed straight state.

**Key words.** twirling, whirling, overwhirling, immersed boundary method

**AMS subject classifications.** 65-04, 65M06, 76D05, 76M20

**DOI.** 10.1137/S1064827502417477

## 1. Introduction.

Dynamics of a rotationally forced filament with twist and bend elasticity at zero Reynolds number has been studied in [1]. These authors consider a slender elastic filament in a fluid of viscosity $\mu$, rotated at one end with the other end free, and assume that its centerline is inextensible. Analytical and numerical methods reveal two dynamical regimes of motion depending on the rotation rate: *twirling*, in which the straight but twisted rod rotates about its centerline, and *whirling*, in which the centerline of the rod writhes and crankshafts around the rotation axis in a steady state. A critical frequency, $\omega_c$, separates whirling from twirling. In this paper, we present simulations of the same physical situation by the immersed boundary (IB) method. The IB method is useful for biofluid mechanical problems to simulate fluid-structure interaction in a viscous incompressible fluid. No approximations such as slender body theory [2] or small deformation are needed when the IB method is used. The IB method was developed to study flow patterns around heart valves [3, 4, 5] and has been applied to many problems of computational fluid dynamics [6, 7, 8, 9, 10, 11].

The computational model we are dealing with here is an elastic and neutrally buoyant filament having microarchitecture motivated by bacterial flagella [12, 13]. It is composed of inner and outer layers with motors on the outer layer at the bottom. We assume that the fluid is governed by the Navier–Stokes equations [14, 15, 16] at a very low but nonzero Reynolds number.

As in [1], we find a critical rotation frequency $\omega_c$, below which the straight state of the filament is stable. When the rotation rate of the filament is above $\omega_c$, however, we find a new phenomenon, which we call *overwhirling*. Overwhirling is the motion in which the tip of filament "falls down" and rotates around its rotation axis in a steady state. We notice that the behavior of filament is very sensitive to the spinning rate

---

[*] Received by the editors November 7, 2002; accepted for publication (in revised form) August 29, 2003; published electronically June 25, 2004. This work was supported by the NIH under research grant R01 GM59875-01A1. Computation was performed in part on the SGI origin 2000 computer at the NCSA under a grant of computer time MCA93S004P from the National Resource Allocation Committee and, in part, at the Applied Mathematics Laboratory, New York University, using immersed boundary software [28] written primarily by Nathaniel Cowen and visualization software [29] written by David McQueen.

http://www.siam.org/journals/sisc/25-6/41747.html

[†] Courant Institute of Mathematical Sciences, New York University, 251 Mercer St., New York, NY 10012 (limsk@cims.nyu.edu, peskin@cims.nyu.edu).

near the critical frequency. Unlike [1], we never find stable filament configurations that are close to the straight state when $\omega > \omega_c$. The bifurcation appears to be subcritical [17].

**2. Equations of motion.** The purpose of this section is to describe the equations of motion. We regard the fluid as incompressible and viscous, and the filament as an elastic structure immersed in this fluid. The notation used here will be defined after the equations have been stated.

Immersed boundary equations (Lagrangian form):

$$\mathbf{F}_{\mathrm{e}} = -\frac{\delta E}{\delta \mathbf{X}}, \tag{2.1}$$

$$\mathbf{F}_{\mathrm{mot}} = c\mathbf{T}_{\mathrm{mot}}, \tag{2.2}$$

$$\mathbf{F} = \mathbf{F}_{\mathrm{e}} + \mathbf{F}_{\mathrm{mot}}. \tag{2.3}$$

Fluid equations (Eulerian form):

$$\rho\left(\frac{\partial \mathbf{u}}{\partial t} + \mathbf{u}\cdot\nabla\mathbf{u}\right) = -\nabla p + \mu\nabla^2\mathbf{u} + \mathbf{f}, \tag{2.4}$$

$$\nabla\cdot\mathbf{u} = 0. \tag{2.5}$$

Interaction equations:

$$\mathbf{f}(\mathbf{x},t) = \int \mathbf{F}(q,r,s,t)\,\delta(\mathbf{x}-\mathbf{X}(q,r,s,t))dqdrds, \tag{2.6}$$

$$\frac{\partial \mathbf{X}(q,r,s,t)}{\partial t} = \mathbf{u}(\mathbf{X}(q,r,s,t)) \tag{2.7}$$

$$= \int \mathbf{u}(\mathbf{x},t)\,\delta(\mathbf{x}-\mathbf{X}(q,r,s,t))\mathbf{dx}. \tag{2.8}$$

The IB equations involve several unknown functions of $(q,r,s,t)$, where $(q,r,s)$ are moving curvilinear coordinates and $t$ is the time. These unknown functions are $\mathbf{X}(q,r,s,t)$, which describes the motion of the IB and its configuration at any time; $\mathbf{F}_{\mathrm{e}}(q,r,s,t)$, which is the elastic force density (with respect to $dqdrds$) derived from $\mathbf{X}$ in the manner described by (2.1) and in more detail below; and $\mathbf{F}_{\mathrm{mot}}(q,r,s,t)$, which is the motor force density acting in the tangential direction $\mathbf{T}_{\mathrm{mot}}(q,r,s,t)$ near the bottom of the filament only.

In (2.1), $\delta E/\delta\mathbf{X}$ is the variational derivative of the elastic energy functional $E[\ ]$. The variational derivative is implicitly defined as follows:

$$\lim_{\epsilon\to 0}\frac{d}{d\epsilon}E[\mathbf{X}+\epsilon\mathbf{Y}] = \int \frac{\delta E}{\delta\mathbf{X}}(q,r,s,t)\cdot\mathbf{Y}(q,r,s,t)dqdrds. \tag{2.9}$$

The fluid equations are the Navier–Stokes equations of a viscous incompressible fluid. They involve several unknown functions of $(\mathbf{x},t)$, where $\mathbf{x} = (x_1,x_2,x_3)$ are fixed Cartesian coordinates. These unknown functions are the fluid velocity vector $\mathbf{u}(\mathbf{x},t)$, the fluid pressure $p(\mathbf{x},t)$, and the applied force density $\mathbf{f}(\mathbf{x},t)$. The constant parameters $\rho$ and $\mu$ in the fluid equations are the fluid density and the fluid viscosity, respectively.

We use the Navier–Stokes equations rather than the Stokes equations even though the Reynolds number is essentially zero and inertial effects are entirely negligible in

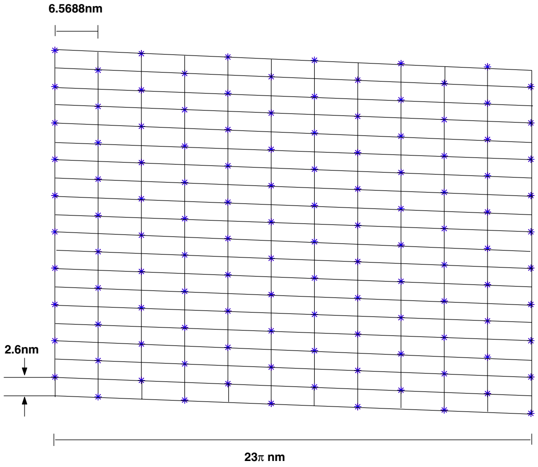

FIG. 1. *Radial projection of the surface lattice of the filament.*

this application. The nature of our numerical scheme is such that this does no harm (see below).

Finally, the interaction equations connect the Lagrangian and Eulerian variables. Both equations involve the three-dimensional Dirac delta function (not to be confused with variational $\delta$ in (2.1) and (2.9)):

$$\delta(\mathbf{x}) = \delta(x_1)\delta(x_2)\delta(x_3), \tag{2.10}$$

which expresses the local character of the interaction. The first of the interaction equations describes the relationship between the two corresponding force densities $\mathbf{f}(\mathbf{x}, t)d\mathbf{x}$ and $\mathbf{F}(q, r, s, t)dqdrds$. Equations (2.7) and (2.8) are the no-slip condition of a viscous fluid, which says that the boundary moves at the local fluid velocity. Each of the interaction equations takes the form of an integral transformation in which the kernel is $\delta(\mathbf{x} - \mathbf{X}(q, r, s, t))$.

## 3. Computational structure of filament.

Because this work is part of a larger project modeling bacterial locomotion, we choose a filament structure that mimics that of a real bacterial flagellum, except that here the unstressed configuration of the flagellar axis is straight rather than helical. (Such straight flagella actually arise as mutations [18, 19].)

A three-dimensional model for filament structure inspired by the bacterial flagellar filament such as that of *E. coli* [12, 13] is a flexible cylindrical tube with two layers, corresponding to the outer surface and inner surface of the hollow flagellum. It has a filament diameter of 23 nm throughout the length and a hollow central channel with a diameter of about 8.9 nm. There is a motor at the bottom.

We present a diagram showing the surface lattice of the filament (see Figure 1). Its radial projection consists of the basic (one-start) helix and 11 protofilaments, which are parallel to the filament axis. The term *start* denotes the number of helices which can account for all of the subunits in the filament.

Each layer of the filament is composed of springs which have connections in eight directions within each layer (solid lines in Figure 2), and there are also connections between the outer and inner layer with pairs of P-P0, P-P1,..., P-P8, where P and P0

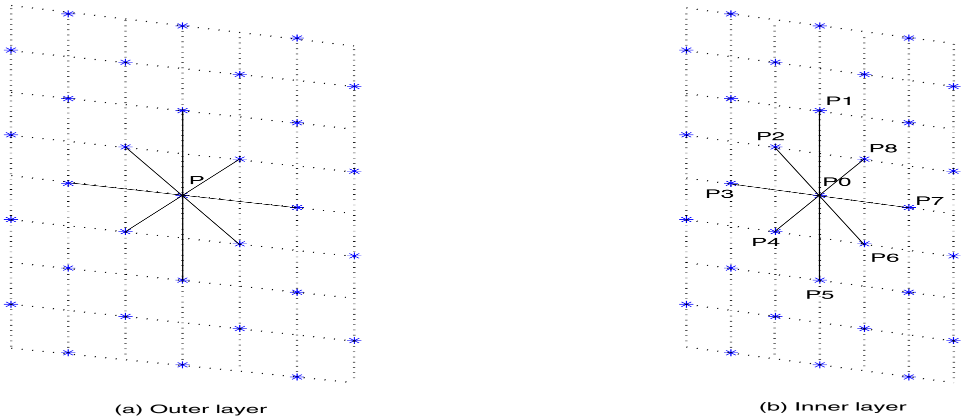

(a) Outer layer

(b) Inner layer

Fig. 2. (a) *Some part of radial projection of outer layer and* (b) *corresponding part of radial projection of inner layer: Asterisks represent lattice points,* P *and* P0 *are corresponding boundary points in the two layers, solid lines are all possible springs within each of the two layers starting from points* P *and* P0*. Note that these springs connect the points* P *and* P0 *to their nearest neighbors in the eight chosen directions within their own layers. For springs connecting one layer to another, see Figure* 3.

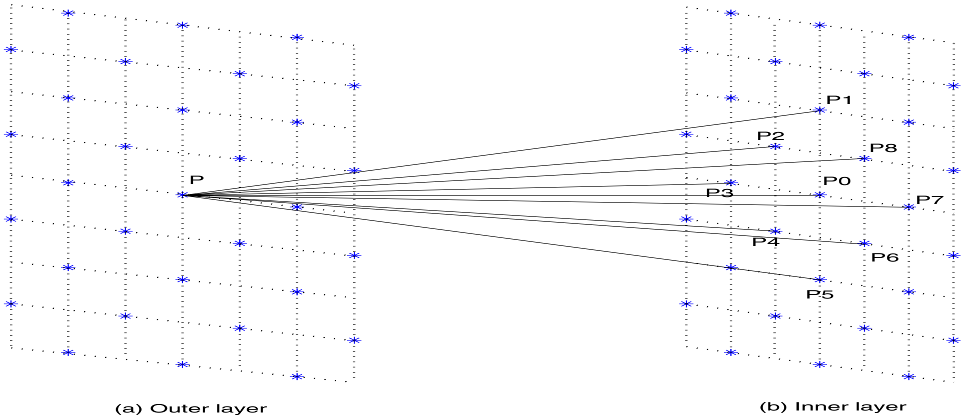

(a) Outer layer

(b) Inner layer

Fig. 3. *Different types of springs between outer and inner layer, showing all possible links which start from one point on the outer layer.*

are corresponding boundary points on the two layers and P1, P2,. . . , P8 are boundary points near P0 in its layer (see Figure 3). In the motor part, we connect the points on the inner layer to fixed points in the symmetry axis of the cylinder by stiff springs. This has the effect that the motor end of the filament seems to be attached to a substratum.

Figures 4 and 5 show all of the springs in the projection seen by looking along the axis of the filament. Figure 4 shows the nonmotor part, whereas Figure 5 shows the motor part. These springs that hold the motor in space do not interfere with the free rotation of the motor part of the filament about its symmetry axis. Rotation of the motor and hence of the whole filament is generated by a torque applied to the motor part.

We need to model an elastic filament whose equilibrium configuration is that of a

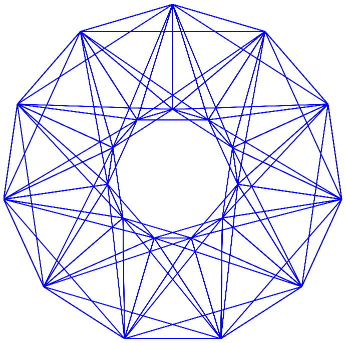

FIG. 4. *Projection of the straight filament looking along its axis, nonmotor part.*

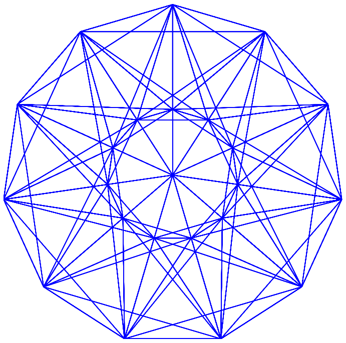

FIG. 5. *Projection of the motor part. Points on the axis are fixed in space.*

straight cylinder. This is done by putting the filament into such a straight cylindrical configuration, and then setting the rest length (see next section) of each elastic link equal to whatever length that link actually has in the chosen configuration. The effect of this choice of rest lengths is that the chosen configuration will be one of minimum (in fact, zero) energy, i.e., a state of mechanical equilibrium.

We do not, however, use the equilibrium configuration as the initial configuration of the filament. The equilibrium configuration has axial symmetry, but our goal is to study the *stability* of the axially symmetric motions, which undoubtedly exist for all rotation rates. To do this, we need to use an initial condition which is at least slightly perturbed away from axial symmetry, i.e., bent. The question will be whether the bent state relaxes back towards a straight state, or whether the bend persists or even grows, at different rotation rates.

We use a cubic box whose length is 20 times the diameter of the filament and put our perturbed filament into this box. Figures 6 and 7 show side views of straight and bent filament, respectively. When the filament is viewed from its nonmotor end, it turns counterclockwise. Even though the direction of rotation could, in principle, matter, since the helical architecture of the filament has a specific handedness, we have checked that virtually identical results are obtained in practice when the direction of rotation of the filament is reversed.

## 4. The immersed boundary (IB) method.

The equations of motion are solved by the IB method [5]. The algorithm for the numerical solution of (2.1)–(2.8)

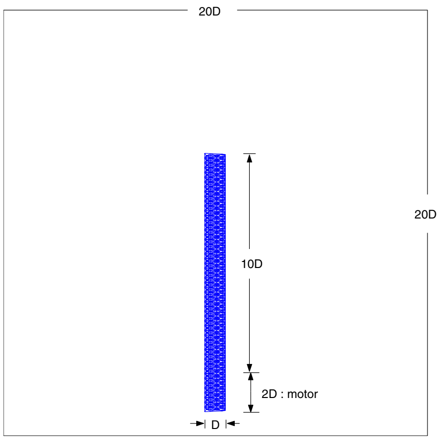

FIG. 6. *Side view of straight filament whose diameter is* $D$ *in the computational domain, a periodic cube with period* $20D$.

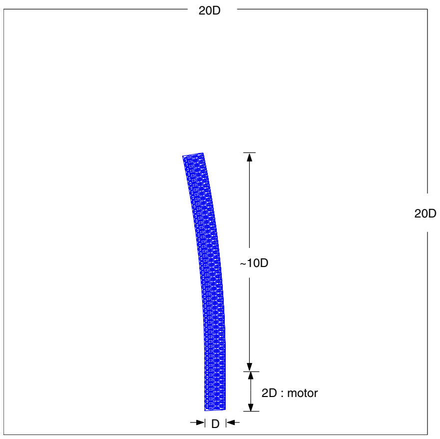

FIG. 7. *Side view of the initial configuration for the computational experiments.*

will be described in this section.

First, we discuss discretization. Let time proceed in steps of duration $\triangle t$, and use a superscript $n$ as the time step index, so that $\mathbf{u}^n$ denotes the whole fluid velocity field at time $t = n\triangle t$, and similarly for all other variables.

The spatial discretization for Eulerian (fluid) variables is different from that of the Lagrangian (IB) variables. For the fluid variables such as $\mathbf{u}$, $p$, and $\mathbf{f}$, we use a fixed periodic cubic lattice of mesh width $h$ and period $m$ in all three space directions. This lattice, denoted $g_{h,m}$ is formally defined as follows:

$$g_{h,m} = \{\mathbf{x} : \mathbf{x} = \mathbf{j}h,\ \mathbf{j} \in \mathcal{Z}_m^3\}, \tag{4.1}$$

where

$$\mathcal{Z}_m = \{0, 1, \ldots, m-1\} \tag{4.2}$$

and arithmetic on $\mathcal{Z}_m$ is understood to be modulo $m$.

Spatial discretization of the IB is accomplished by the discrete elastic structure described in the previous section. Let the points of this structure be numbered in some arbitrary order $k = 1, 2, \ldots, K$. Then $\mathbf{X}_k^n$ denotes the position at time step $n$ of the IB point whose label is $k$. Similarly, $\mathbf{F}_k^n$ is the force applied to the fluid by that same boundary point, at that time step. Note that $\mathbf{F}_k^n$ is a force, not a force density. Thus

$$\mathbf{F}_k^n \sim \mathbf{F}(q, r, s, n\triangle t) dq dr ds. \tag{4.3}$$

Because of this, we do not have any factors like $\triangle q \triangle r \triangle s$ in our algorithm or code.

The elastic part, $(\mathbf{F}_{\mathrm{e}})_k^n$, of the discrete IB force can be calculated from the discrete elastic energy $E(\mathbf{X}_1, \ldots, \mathbf{X}_K)$ by differentiation:

$$(\mathbf{F}_{\mathrm{e}})_k^n = -\frac{\delta E}{\delta \mathbf{X}_k}(\mathbf{X}_1^n, \ldots, \mathbf{X}_K^n). \tag{4.4}$$

This vector equation is shorthand for

$$(F_{\mathrm{e}})_{k\alpha}^n = -\frac{\partial E}{\partial X_{k\alpha}}(\mathbf{X}_1^n, \ldots, \mathbf{X}_K^n), \tag{4.5}$$

where $\alpha = 1, 2, 3$ is an index denoting the space direction.

To keep track of the topological structure of the discretized immersed elastic boundary, it is useful to introduce the notion of a link table [4, 20]. Let the elastic links that connect some of the pairs of boundary points (but not all possible pairs!) be numbered in arbitrary order $l = 1, 2, \ldots, l_{\max}$. Let $k_1(l)$ and $k_2(l)$ be the indices of the points that are connected by link $l$. (If $k_1(l)$ and $k_2(l)$ are interchanged, it makes no difference.) Then link properties such as stiffness and rest length can be regarded as functions of $l$, and the elastic forces $((\mathbf{F}_{\mathrm{e}})_1^n \cdots (\mathbf{F}_{\mathrm{e}})_K^n)$ can be much more efficiently computed by an algorithm that loops over $l$ than by an algorithm that loops over $k$.

The elastic energy function that we use in this work is as follows:

$$E(\mathbf{X}^n) = \sum_l \frac{S_0}{2}(\|\mathbf{X}_{k_1(l)}^n - \mathbf{X}_{k_2(l)}^n\| - L_0(l))^2. \tag{4.6}$$

Thus each link $l$ represents a linear (Hookean) spring with stiffness $S_0$ (the same for all links, for simplicity) and rest length $L_0(l)$. The method used to choose $L_0(l)$ was described in the previous section.

In addition to the elastic force $(\mathbf{F}_{\mathrm{e}})_k^n$ which is derived from $E$ in the manner described above, we also apply another force $\mathbf{F}_{\mathrm{mot}}$ to the outer layer of the motor part of the filament. Naturally, this force will vanish at all the boundary points except for motor points, where it is given by

$$(\mathbf{F}_{\mathrm{mot}})_k^n = c(\mathbf{T}_{\mathrm{mot}})_k^n, \tag{4.7}$$

where $\mathbf{T}_{\mathrm{mot}}^n$ is the unit tangent vector of the outer layer of the motor part at time step $n$. Therefore the total force $\mathbf{F}^n$ at time step $n$ is the sum of elastic spring forces and motor forces, i.e.,

$$\mathbf{F}_k^n = (\mathbf{F}_{\mathrm{e}})_k^n + (\mathbf{F}_{\mathrm{mot}})_k^n. \tag{4.8}$$

Once the total force $\mathbf{F}_k^n$ is known, the next step of the IB algorithm is to apply these forces to the computational grid of the fluid:

$$\mathbf{f}^n(\mathbf{x}) = \sum_k \mathbf{F}_k^n \delta_h(\mathbf{x} - \mathbf{X}_k^n), \tag{4.9}$$

where $\mathbf{x} \in g_{h,m}$ and $\delta_h$ is a smoothed approximation to the three-dimensional Dirac $\delta$-function and is of the form

$$\delta_h(\mathbf{x}) = \frac{1}{h^3}\phi\left(\frac{x_1}{h}\right)\phi\left(\frac{x_2}{h}\right)\phi\left(\frac{x_3}{h}\right), \tag{4.10}$$

where $\mathbf{x} = (x_1, x_2, x_3)$ and the function $\phi$ is given by

$$\phi(r) = \begin{cases} \dfrac{3 - 2|r| + \sqrt{1 + 4|r| - 4r^2}}{8} & \text{if } |r| \le 1, \\ \dfrac{5 - 2|r| - \sqrt{-7 + 12|r| - 4r^2}}{8} & \text{if } 1 \le |r| \le 2, \\ 0 & \text{if } |r| \ge 2. \end{cases}$$

The next step is to solve the following system of equations for $(\mathbf{u}^{n+1}, p^{n+1})$:

$$\rho\left(\frac{\mathbf{u}^{n+1} - \mathbf{u}^n}{\triangle t} + \sum_{\alpha=1}^{3} u_\alpha^n D_\alpha^\pm \mathbf{u}^n\right) + \mathbf{D}^0 p^{n+1} = \mu \sum_{\alpha=1}^{3} D_\alpha^+ D_\alpha^- \mathbf{u}^{n+1} + \mathbf{f}^n, \tag{4.11}$$

$$\mathbf{D}^0 \cdot \mathbf{u}^{n+1} = 0. \tag{4.12}$$

Here, $\mathbf{D}^0$ is the central-difference approximation to $\nabla$ defined by $\mathbf{D}^0 = (D_1^0, D_2^0, D_3^0)$. The forward $D^+$, the backward $D^-$, and centered $D^0$ difference operator are defined in the standard way. Thus $\mathbf{D}^0 p$ approximates $\nabla p$ and $\mathbf{D^0} \cdot \mathbf{u}$ approximates $\nabla \cdot \mathbf{u}$. The expression $\sum_{\alpha=1}^{3} D_\alpha^+ D_\alpha^-$, which appears in the viscous term, is a difference approximation to the Laplace operator, and the expression $\sum_{\alpha=1}^{3} u_\alpha D_\alpha^\pm$, where

$$u_\alpha D_\alpha^\pm = \begin{cases} u_\alpha D_\alpha^+, & u_\alpha < 0, \\ u_\alpha D_\alpha^-, & u_\alpha > 0, \end{cases}$$

is an upwind difference approximation to $\mathbf{u} \cdot \nabla$.

Now we use the fast Fourier transform (FFT) algorithm [21] to solve (4.11)–(4.12) for the unknowns $(\mathbf{u}^{n+1}, p^{n+1})$. Note that these are linear equations (nonlinear terms involve known quantities at time level $n$ only) with constant coefficients on a periodic domain.

Once $\mathbf{u}^{n+1}(\mathbf{x})$ has been determined, the boundary points are moved at the local fluid velocity in this new velocity field. This is done by the following interpolation scheme:

$$\frac{\mathbf{X}_k^{n+1} - \mathbf{X}_k^n}{\triangle t} = \sum_{\mathbf{x}} \mathbf{u}^{n+1}(\mathbf{x})\delta_h(\mathbf{x} - \mathbf{X}_k^n)h^3, \tag{4.13}$$

where $\sum_{\mathbf{x}}$ denotes the sum over the computational lattice $\mathbf{x} \in g_{h,m}$.

In summary, the IB method proceeds as follows: at the beginning of each time step $n$ we have the fluid velocity field $\mathbf{u}^n$ and the configuration of the IB $\mathbf{X}^n$. In order to update these values to the next time step we

- compute the elastic force $\mathbf{F}_{\mathrm{e}}^n$ from the boundary configuration, and add the motor force $\mathbf{F}_{\mathrm{mot}}^n$ to obtain $\mathbf{F}^n$;
- spread the boundary force to the grid to determine the Eulerian force $\mathbf{f}^n$ acting on the fluid;
- solve the discretized Navier–Stokes equations for $\mathbf{u}^{n+1}$ and $p^{n+1}$;

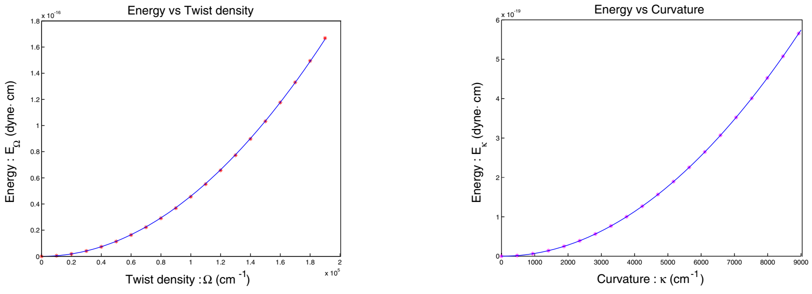

(a) (b)

FIG. 8. (a) *Energy vs. twist density.* (b) *Energy vs. curvature.*

- interpolate the new fluid velocity field to the IB points and move the boundary at this local fluid velocity.

The form of the IB method that we have just described is first order accurate in space and time and has the numerical viscosity associated with upwind differences of the nonlinear terms. This is not a problem at the low Reynolds number of the present application, in which the nonlinear terms are negligible in any case. For improved accuracy and reduced numerical viscosity, the IB method described in [22, 23, 24] is currently recommended.

**5. “Measuring” the bending modulus and twist modulus.** For comparison with the theory of [1] it is important to know the macroscopic bending modulus $A$ of our elastic filament. For completeness, we also evaluate the twist modulus $C$, although it does not appear in the formula for the critical frequency derived in [1]. We expect that $A$ and $C$ will both be proportional to the stiffness constant $S_0$, but that the constants of proportionality will depend in a complicated way on the structural details of the filament. Instead of trying to evaluate these moduli analytically, we resort to “measurement.”

An elastic filament is characterized by its bending modulus $A$ and twist modulus $C$ as well as its radius $a_{\mathrm{f}}$ and length of filament $L_{\mathrm{f}}$.

In this section we describe how to measure the bending modulus and twist modulus. In order to get both quantities we start with a straight filament standing at the origin with the z-axis as the axis of the filament.

First, consider the simpler case of twist modulus. Let $\Omega$ be twist density and $\theta$ be twist angle defined by $\theta = \Omega z$. Given twist density $\Omega$, rotate the points $(x, y, z)$ of the straight filament about $(0, 0, z)$ by the angle of $\theta = \Omega z$, i.e.,

$$(x, y, z) \mapsto (x\cos(\Omega z) - y\sin(\Omega z), x\sin(\Omega z) + y\cos(\Omega z), z), \tag{5.1}$$

and then with this twisted but straight structure, evaluate the energy $E_\Omega$ by (4.6). Thus we have a set of pairs $(\Omega, E_\Omega)$ for the different values of twist density $\Omega$, which are shown in Figure 8(a) as dots. Since the energy corresponding to twist density $\Omega$ is an integral over arclength along the filament centerline [25, 26, 27], and since $\Omega$ is constant in our case,

$$E_\Omega = \frac{C}{2}\Omega^2 L_{\mathrm{f}}. \tag{5.2}$$

To find the best fit of this formula to the data points $(\Omega, E_\Omega)$, we use the method of least squares to determine the twist modulus $C$.

Now consider the bending modulus $A$. First, we define a centerline for the bent filament as the curve

$$\boldsymbol{\alpha}(s) = (0, R - R\cos(s/R), R\sin(s/R)), \quad s \geq 0, R > 0, \tag{5.3}$$

where $R$ is desired radius of curvature, so that $\kappa = 1/R$ is the curvature. Next, we introduce three vectors $\{\mathbf{t}, \mathbf{n}, \mathbf{b}\}$ which form a right-handed orthonormal triad at any point $s$ along the curve:

$$\mathbf{t} = \frac{\boldsymbol{\alpha}'(s)}{|\boldsymbol{\alpha}'(s)|} = (0, \sin(s/R), \cos(s/R)), \tag{5.4}$$

$$\mathbf{n} = \frac{\mathbf{t}'(s)}{|\mathbf{t}'(s)|} = (0, \cos(s/R), -\sin(s/R)), \tag{5.5}$$

$$\mathbf{b} = \mathbf{t} \times \mathbf{n} = (-1, 0, 0), \tag{5.6}$$

where $\mathbf{t}$ is the tangent vector of $\boldsymbol{\alpha}$ at $s$, $\mathbf{n}$ is the principal normal vector, and $\mathbf{b}$ is the (constant) binormal vector. Now recall the straight filament. Each point $(x, y, z)$ of the straight filament has its own angle $\beta$ obtained by projection of the point to the $xy$-plane, where $\tan\beta = \frac{y}{x}$, and also its own distance from the axis given by $r = \sqrt{x^2 + y^2}$. The way to get the bent filament of curvature $\kappa = 1/R$ is as follows:

$$(x, y, z) \mapsto r(\mathbf{n}\cos(-\beta) + \mathbf{b}\sin(-\beta)) + (0, R - R\cos(z/R), R\sin(z/R)), \tag{5.7}$$

where $\beta = \arctan(y/x)$ and $r = \sqrt{x^2 + y^2}$ and where $\mathbf{n}$ and $\mathbf{b}$ are given by (5.5) and (5.6). Substituting the expressions for $\mathbf{n}$ and $\mathbf{b}$, we get $(x, y, z) \mapsto (x', y', z')$, where

$$x' = r\sin\beta, \tag{5.8}$$

$$y' = r\cos(z/R)\cos\beta + R - R\cos(z/R), \tag{5.9}$$

$$z' = -r\sin(z/R)\cos\beta + R\sin(z/R). \tag{5.10}$$

Geometrically, each of these transformed points lies on the circle of radius $r$ around the bent centerline, and the plane including the circle is perpendicular to the bent centerline. As in the case of evaluating the twist modulus, we apply the deformation given by (5.8)–(5.10) to every point $\mathbf{X}_k$ of the model filament, starting from its zero-energy configuration as constructed in section 3. As the curvature $\kappa$ varies, we evaluate the energy $E_\kappa$ of the bent structure by (4.6) so that we may have data points $(\kappa, E_\kappa)$ (dots in Figure 8(b)). Since the energy for curvature $\kappa$ is

$$E_\kappa = \frac{A}{2}\kappa^2 L_{\mathrm{f}}, \tag{5.11}$$

we fit this formula to the data points $(\kappa, E_\kappa)$ to get bending modulus $A$ by using the method of least squares.

Note that the units of $\kappa$ and $\Omega$ are $\mathrm{cm}^{-1}$.

From the above procedure, we have

$$A = (6.1278 \times 10^{-18}\,\mathrm{cm}^3)S_0 \tag{5.12}$$

and

$$C = (3.9753 \times 10^{-18}\,\mathrm{cm}^3)S_0. \tag{5.13}$$

Table 1
*Physical parameters.*

| Physical parameters | |
|---|---|
| Fluid density, $\rho$ | $1\mathrm{g/cm}^3$ |
| Fluid viscosity, $\mu$ | $0.01\mathrm{g/cm}\cdot\mathrm{s}$ |
| Length of filament, $L_\mathrm{f}$ | $278.2\,\mathrm{nm}$ |
| Radius of filament, $a_\mathrm{f}$ | $11.5\,\mathrm{nm}$ |
| Reynolds number, $\mathrm{Re} = \frac{\rho(2a_\mathrm{f})(a_\mathrm{f}\omega)}{\mu}$ | $1\times10^{-9}$ |

As is clear from (5.12) and (5.13), the bending modulus $A$ and the twist modulus $C$ are not independent, since both are determined by the single parameter $S_0$. The relationship between them is a consequence of the particular structure, inspired by that of bacterial flagella, that we have chosen. Even within the framework of this particular structure, however, one could, if desired, alter the relationship between $A$ and $C$ by choosing different stiffnesses for the different kinds of links in the model filament.

In our experiment we choose the stiffness $S_0 = 1\times10^{-4}\,\mathrm{dyne/cm}$; therefore the bending modulus is $6.1278\times10^{-22}\,\mathrm{dyne}\cdot\mathrm{cm}^2$ and the twist modulus is $3.9753\times10^{-22}\mathrm{dyne}\cdot\mathrm{cm}^2$. Note that this choice is made for comparison with [1] and *not* to model a real bacterial flagellum.

As pointed out by an anonymous reviewer, the methods of this section do not address the issue of bend-twist coupling, i.e., whether there might be a term in the elastic energy density of the form $B\kappa\Omega$. Such a term may indeed be present because the helical architecture of our model filament has a definite handedness. As mentioned above, however, we have tried spinning the filament in both directions to see whether we can detect any difference in behavior related to the handedness of the filament, and we cannot. This suggests that bend-twist coupling does not play a significant role in the present study.

**6. Results and discussion.** Since the research described here was inspired by [1], we summarize the main results of that paper for comparison with results reported below. Let $\omega$ be the angular frequency of rotation of the filament about its centerline. The principal result of [1] is the existence of a critical frequency $\omega_c$ at which a change in stability occurs. For $\omega < \omega_c$, the motion known as "twirling" is stable. In twirling, the centerline of the filament is straight and the filament (although twisted) rotates as a rigid body about its centerline at the angular velocity $\omega < \omega_c$. For $\omega > \omega_c$, the twirling motion is unstable and is replaced, according to [1], by a more complicated motion known as "whirling." In whirling, the centerline of the filament is bent, and the centerline rotates around the symmetry axis of the whole system at an angular frequency $\chi$ which is different from $\omega$. The motion of the filament is therefore *not* that of a rigid body. For $\omega-\omega_c$ small and positive, the prediction of [1] is that the filament will be only *slightly* bent, the amplitude of the bend increasing with $\sqrt{\omega-\omega_c}$.

According to [1] the critical frequency $\omega_c$ and crankshafting frequency $\chi_c$ when $\omega-\omega_c$ is small and positive are given approximately by

$$\omega_c \simeq 0.563\left(\frac{a_\mathrm{f}}{L_\mathrm{f}}\right)^2\frac{E_\mathrm{Y}}{\mu} = 0.563\frac{4}{\pi}\left(\frac{1}{a_\mathrm{f}L_\mathrm{f}}\right)^2\frac{A}{\mu}, \tag{6.1}$$

$$\chi_c \simeq 20.9\left(\frac{a_\mathrm{f}}{L_\mathrm{f}}\right)^2\omega_c. \tag{6.2}$$

Table 2
*Motor frequency and dynamical motions.*

| motor frequency | dynamical motion |
|---|---|
| 1.6949 Hz | twirling |
| 2.7397 Hz | twirling |
| 2.7855 Hz | twirling |
| 2.8249 Hz | overwhirling |
| 2.9126 Hz | overwhirling |
| 3.4364 Hz | overwhirling |

In these formulae, $a_\mathrm{f}$ and $L_\mathrm{f}$ are radius and length of the filament, respectively, $E_\mathrm{Y}$ is the Young's modulus of the filament material, and $\mu$ is the dynamic viscosity of the surrounding fluid. The constant $A$ is the bending modulus of the filament (see previous section), which is related to the other parameters by $A = \frac{\pi}{4} a_\mathrm{f}^4 E_\mathrm{Y}$.

Inserting the numerical values used in this work ($a_\mathrm{f} = 1.15 \times 10^{-6}\,\mathrm{cm}, L_\mathrm{f} = 2.782 \times 10^{-5}\,\mathrm{cm}, A = 6.1278 \times 10^{-22}\,\mathrm{g} \cdot \mathrm{cm}^3/\mathrm{s}^2, \mu = 0.01\,\mathrm{g}/(\mathrm{cm} \cdot \mathrm{s})$) yields the following predicted values for $\omega_c$ and $\chi_c$:

$$\omega_c = 62.0299/s = 9.8724\,\mathrm{Hz}, \tag{6.3}$$

$$\chi_c = 3.2020/s = 0.5096\,\mathrm{Hz}. \tag{6.4}$$

(Recall that $\omega$ and $\chi$ are angular frequencies, which must be divided by $2\pi$ to get frequencies in Hz = cycles per second.)

In our numerical experiments, we find a critical frequency $\omega_c$ which is about 3.5 times smaller than the predicted value $\omega_c$ above. For low turning rates $\omega < \omega_c$, the initially bent state of the filament comes back towards a straight state, and the filament rotates about its centerline as a rigid body; i.e., the twirling motion is stable as in [1]. However, for $\omega > \omega_c$, we find a new phenomenon which we call *overwhirling.* In overwhirling, the bend of the filament increases dramatically to the extent that the free end of the filament goes below the motor. Also, although we do see the crankshafting phenomenon while the bend of the filament is small, the crankshafting frequency increases as the bend increases, and it appears that the crankshafting frequency $\chi$ may even approach the motor frequency $\omega$ once overwhirling becomes fully developed. (We have not checked this carefully, since very long computer runs would be required.) We never see the steady whirling motion when $\omega > \omega_c$.

Table 2 shows the dynamical motion that results depending on the motor frequency. (Here, the motor frequency is not an input variable but an output variable. After we apply the motor force to the motor part we measure the actual angular frequency of the motor. In order to be reasonable we choose the time interval after the first few seconds and before big changes happen; see Figure 9.)

Note that the critical frequency lies between the rotation rates 2.7855 Hz and 2.8249 Hz, which differ by less than 2%. Since the twirling motion and the overwhirling motion are completely different, this means the behavior of the filament is very sensitive to the rotation rate near the critical frequency $\omega_c$.

Figure 10 shows the twirling motion. The first three snapshots (a)–(c) are side views of the motion, showing that the bent filament becomes straight, and the following six frames (d)–(i) are viewed from the nonmotor part looking along the symmetry axis of the filament. Fluid markers are spread around the filament and leave the trails showing their trajectories.

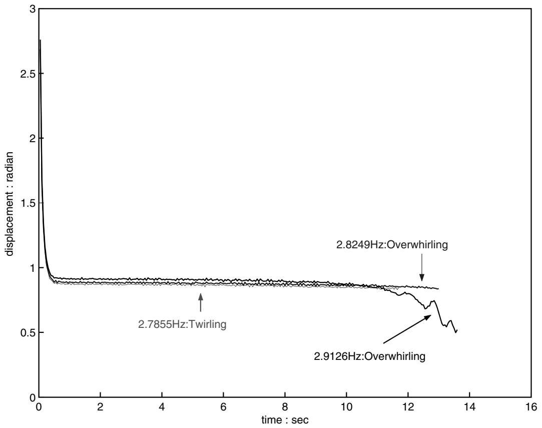

FIG. 9. *Measuring motor frequency.*

Figure 11 shows the overwhirling motion. The free end of the filament lags behind the part closer to the motor end; see the first six frames (a)–(f). Once the free end of the filament "falls down," the motion of the filament continues to be as shown in the last three frames (g)–(i).

To determine the nature of the bifurcation that happens as the motor frequency $\omega$ crosses the critical frequency $\omega_c$, we choose a particular torque such that the motor frequency during twirling was 2.7397 Hz (see Table 2), which is slightly below the critical frequency, and apply this torque to the filament with various initial bends. At the chosen frequency, for small initial bend the filament straightens out into a twirling motion, but for large enough initial bend, the filament goes into an overwhirling motion. Since all parameters are the same except for the initial conditions, this demonstrates *bistability* which is characteristic of a *subcritical* bifurcation [17]. In [1] it is stated that the bifurcation is supercritical and hence that small-amplitude whirling motions are stable for frequencies slightly above the critical frequency. In our study, stable small-amplitude whirling motions are never seen.

One possible reason for the difference between our results and those of [1] is that [1] uses a local model of fluid drag based on slender body theory applied to each segment of the filament separately, without taking into account the interaction between two different parts of the filament through the fluid. That interaction is, of course, included in our simulations. Another possibility, however, suggested by Wolgemuth, is that the discrepancies are most likely because the authors of [1] analyzed the weakly nonlinear theory rather than the full nonlinear problem. Indeed, Wolgemuth has since done fully nonlinear numerical computations concerning the model defined in [1] and has found a stable steady state closely resembling our overwhirling state (unpublished).

One of the features of small-amplitude whirling reported in [1] is the pumping of fluid in the axial direction. This happens because the filament takes on a slightly helical configuration during whirling. Even though whirling does not persist indefinitely in our simulations (it either relaxes to twirling or breaks down into overwhirling), during the interval of time that the motion looks like whirling, we do indeed see the pumping phenomenon, as shown in Figure 12. In this figure, which corresponds to the bistable case described above, the initial bend of the filament is close to the critical initial bend, so that whirling persists for a reasonable amount of time. During this

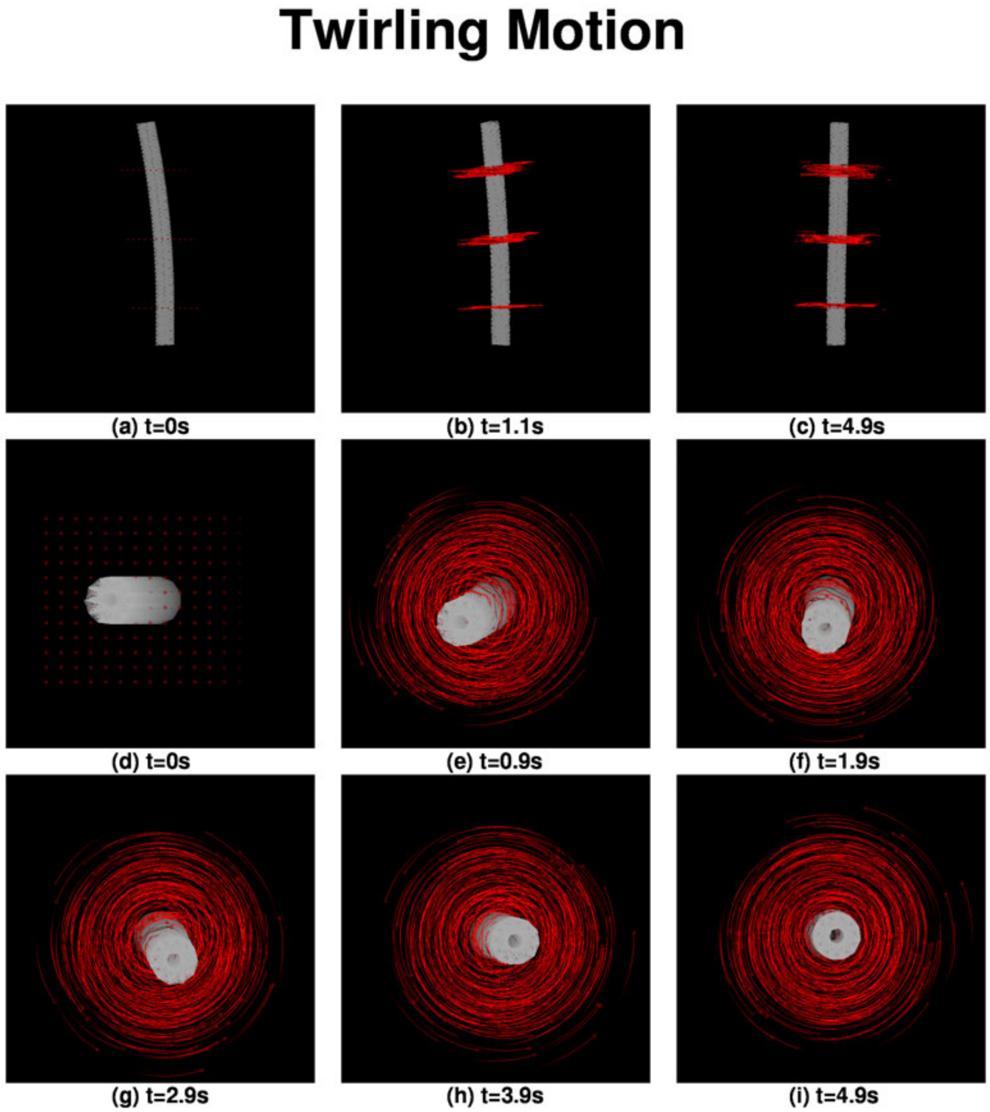

(a) t=0s (b) t=1.1s (c) t=4.9s

(d) t=0s (e) t=0.9s (f) t=1.9s

(g) t=2.9s (h) t=3.9s (i) t=4.9s

Fig. 10. *Twirling motion.*

time, we see that fluid markers are moving up along the filament, which is pumping fluid along its axis. Compare with Figure 10(a)–(c), which shows that fluid markers rotate but stay around the filament.

In all of the studies described so far, the model filament is a network of linear (Hookean) springs. One may wonder whether the results would change qualitatively if nonlinear material properties were considered. In particular, one might think that nonlinear material properties could, by opposing large deformations, stabilize the whirling motion and prevent the sudden transition to overwhirling. To test this hypothesis we considered two different length-tension relationships besides the linear

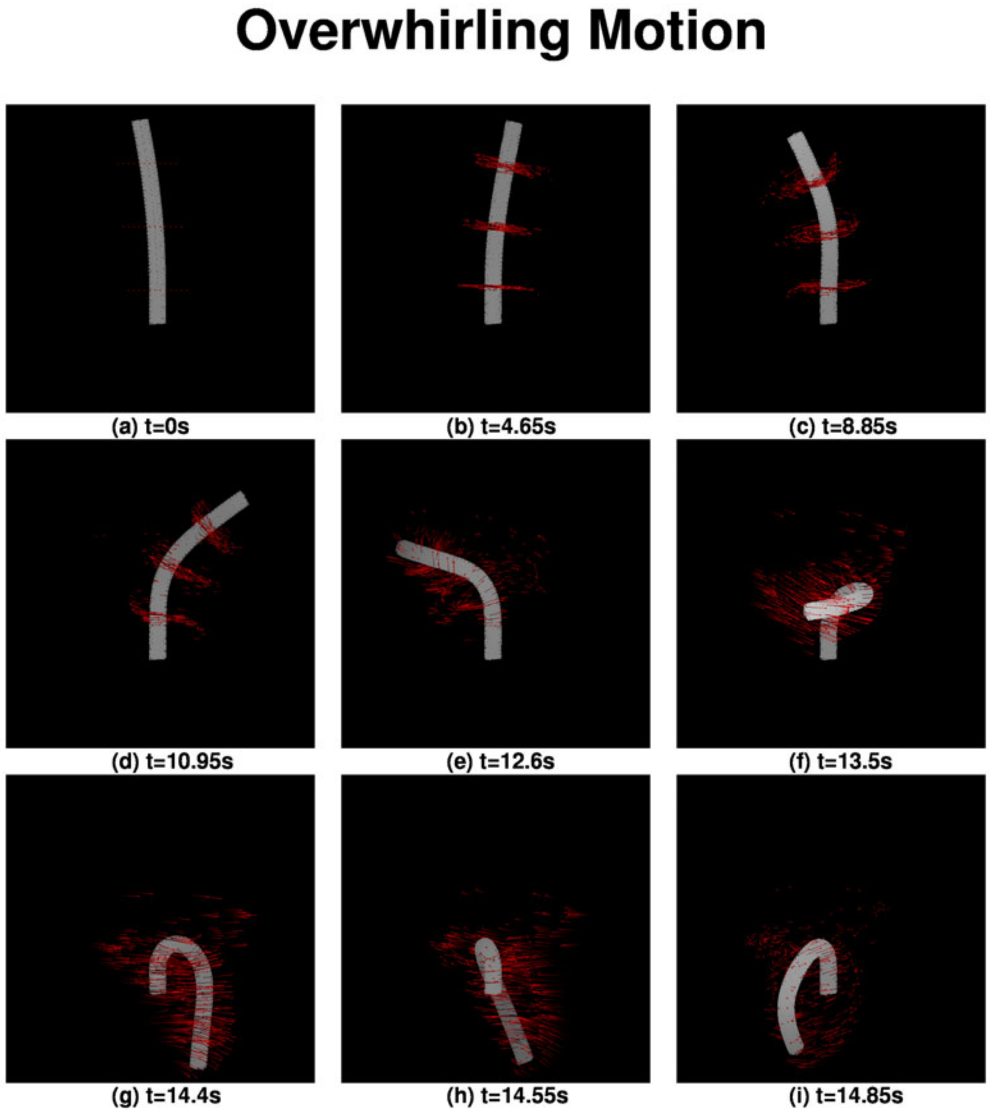
Overwhirling Motion

(a) t=0s (b) t=4.65s (c) t=8.85s

(d) t=10.95s (e) t=12.6s (f) t=13.5s

(g) t=14.4s (h) t=14.55s (i) t=14.85s

Fig. 11. *Overwhirling.*

$T = S_0(L - L_0)$ that was used in the studies reported above. These are

$$T_1 = S_0 \frac{\lambda}{\pi} \tan\left(\frac{\pi}{\lambda}(L - L_0)\right) \tag{6.5}$$

or

$$T_2 = S_0 \lambda \left(\exp\left(\frac{L - L_0}{\lambda}\right) - 1\right), \tag{6.6}$$

where $\lambda$ is an input parameter. Note that $(dT_1/dL)_{L=L_0} = (dT_2/dL)_{L=L_0} = S_0$, so that both of these nonlinear springs have the same resting stiffness as the linear spring.

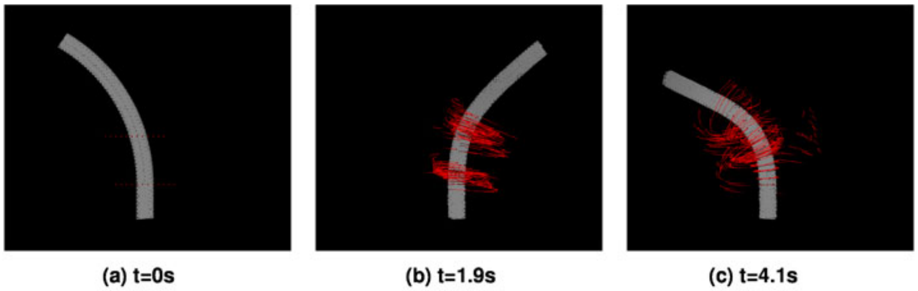

Fig. 12. (a) *Initial configuration,* (b) *and* (c) *are snapshots at time t in seconds. Fluid markers are spread around the filament and show their trajectories.*

Table 3
*Computational parameters.*

| Computational parameters | |
|---|---|
| Fluid grid | $64 \times 64 \times 64$ |
| Computational domain (cubic) | $460\,\mathrm{nm} \times 460\,\mathrm{nm} \times 460\,\mathrm{nm}$ |
| Meshwidth, $h$ | $7.1875\,\mathrm{nm}$ |
| Duration, $\triangle t$ | $5 \times 10^{-6}$ sec |
| Stiffness, $S_0$ | 0.0001 dyne/cm |

For large $\lambda$, both of these springs become approximately linear, and their nonlinearities get more pronounced as $\lambda$ is made smaller. The nonlinear spring described by (6.5) resists both extension and compression more strongly than a comparable linear spring, whereas the nonlinear spring described by (6.6) resists extension more strongly but compression less strongly than a comparable linear spring. Although these changes in material properties can change an overwhirling case into a twirling case, they do not stabilize the whirling motion, and the qualitative fact that we see only twirling or overwhirling remains unchanged.

The computations reported here are very demanding. The principal numerical parameters are summarized in Table 3. A typical computation required $3 \times 10^6$ time steps at 1.26 cpu sec per time step, on an SGI origin 2000 computer, for a total of 43.75 days cpu time. Because of this, it was not practical to refine the computational mesh beyond the $64 \times 64 \times 64$ grid used to obtain the results reported here.

## 7. Summary and conclusion.

This paper uses the immersed boundary (IB) method to study the stability of a spinning elastic filament in a viscous fluid. A structural model of the filament based on the microscopic architecture of bacterial flagella is used. Macroscopic bending and twist moduli of this structure are determined computationally for comparison with other studies such as [1] that are based on these parameters. The coupled equations of motion of the spinning elastic filament and the viscous fluid are formulated and solved by the IB method.

A surprising conclusion of our study is the existence of a sharp transition between two drastically different motions: twirling and overwhirling. In twirling, the filament configuration is straight, but in overwhirling it is bent through more than 180°. We have seen this transition occur as a consequence of change in the spinning frequency of only 2%. Presumably, the transition is sharp and an arbitrarily small change in frequency across the critical frequency would suffice. This large change in amplitude as a consequence of a small change in a bifurcation parameter is the hallmark of a subcritical bifurcation.

We have confirmed the subcritical nature of this bifurcation by demonstrating another of its characteristic features: bistability at spinning frequencies just below the critical frequency. At such a subcritical frequency, we have shown that small-amplitude initial bends relax to twirling, whereas larger amplitude initial bends grow into overwhirling. Thus twirling and overwhirling coexist as possible stable dynamical states in an interval of subcritical spinning frequencies.

**Acknowledgments.** We thank both Nathaniel Cowen and David McQueen not only for the use of their software but also for their kind assistance on many occasions during the course of this research. We are also indebted to Charles Wolgemuth for helpful discussion and for kindly providing unpublished numerical results supportive of our findings.

## REFERENCES

[1] C. W. Wolgemuth, T. R. Powers, and R. E. Goldstein, *Twirling and whirling: Viscous dynamics of rotating elastic filaments*, Phys. Rev. Lett., 84 (2000), pp. 16–23.

[2] J. B. Keller and S. I. Rubinow, *Slender-body theory for slow viscous flow*, J. Fluid Mech., 75 (1976), pp. 705–714.

[3] C. S. Peskin, *Flow patterns around heart valves: A numerical method*, J. Comput. Phys., 10 (1972), pp. 252–271.

[4] C. S. Peskin, *Numerical analysis of blood flow in the heart*, J. Comput. Phys., 25 (1977), pp. 220–252.

[5] C. S. Peskin and D. M. McQueen, *Fluid dynamics of the heart and its valves*, in Case Studies in Mathematical Modeling: Ecology, Physiology, and Cell Biology, H. G. Othmer, F. R. Adler, M. A. Lewis, and J. C. Dallon, eds., Prentice-Hall, Englewood Cliffs, NJ, 1996, pp. 309–337.

[6] L. Fauci and C. S. Peskin, *A computational model of aquatic animal locomotion*, J. Comput. Phys., 77 (1988), pp. 85–108.

[7] L. Zhu and C. S. Peskin, *Simulation of a flapping flexible filament in a flowing soap film by the immersed boundary method*, J. Comput. Phys., 179 (2002), pp. 452–468.

[8] R. Dillon, L. Fauci, and D. Gaver III, *A microscale model of bacterial swimming, chemotaxis and substrate transport*, J. Theor. Biol., 177 (1995), pp. 325–340.

[9] E. Jung and C. S. Peskin, *Two-dimensional simulations of valveless pumping using the immersed boundary method*, SIAM J. Sci. Comput., 23 (2001), pp. 19–45.

[10] E. Givelberg, *Modelling Elastic Shells Immersed in Fluid*, Ph.D. thesis, Mathematics, New York University, 1997; available online at http://www.umi.com/hp/Products/DisExpress.html, order number 9808292.

[11] A. L. Fogelson, *A mathematical model and numerical method for studying platelet adhesion and aggregation during blood clotting*, J. Comput. Phys., 56 (1984), pp. 111–134.

[12] C. J. Jones and S. I. Aizawa, *The bacterial flagellum and flagellar motor: Structure, assembly and function*, Adv. Microb. Physiol., 32 (1991), pp. 109–172.

[13] C. R. Calladine, *Change of waveform in bacterial flagella: The role of mechanics at the molecular level*, J. Mol. Biol., 118 (1978), pp. 457–479.

[14] A. J. Chorin and J. E. Marsden, *A Mathematical Introduction to Fluid Mechanics*, Springer-Verlag, New York, 1993.

[15] Sir J. Lighthill, *Mathematical Biofluiddynamics*, Regional Conference Series in Applied Mathematics 17, SIAM, Philadelphia, 1975.

[16] S. Childress, *Mechanics of Swimming and Flying*, Cambridge Stud. Math. Biol., Cambridge University Press, Cambridge, UK, 1981.

[17] S. H. Strogatz, *Nonlinear Dynamics and Chaos*, Westview Press, Boulder, CO, 2000.

[18] H. Kondoh and M. Yanagida, *Structure of straight flagellar filaments from a mutant of E. coli*, J. Mol. Biol., 96 (1975), pp. 641–652.

[19] N. Nanninga, *Molecular Cytology of E. coli*, Academic Press, New York, 1985, pp. 9–37.

[20] C. S. Peskin and D. M. McQueen, *Modeling prosthetic heart valves for numerical analysis of blood flow in the heart*, J. Comput. Phys., 37 (1980), pp. 113–132.

[21] W. H. Press, B. P. Flannery, S. A. Teukolsky, and W. T. Vetterling, *Numerical Recipes. The Art of Scientific Computing*, Cambridge University Press, Cambridge, UK, 1986, pp. 390–396.

[22] M. C. Lai and C. S. Peskin, *An immersed boundary method with formal second-order accuracy and reduced numerical viscosity*, J. Comput. Phys., 160 (2000), pp. 705–719.

[23] D. M. McQueen and C. S. Peskin, *Heart simulation by an immersed boundary method with formal second-order accuracy and reduced numerical viscosity*, in Proceedings of the ICTAM, 2000.

[24] C. S. Peskin, *The immersed boundary method*, in Acta Numerica, Cambridge University Press, Cambridge, UK, 2002, pp. 1–39.

[25] S. S. Antman, *Nonlinear Problems of Elasticity*, Springer-Verlag, New York, 1995.

[26] I. Keller, *Biological applications of the dynamics of twisted elastic rods*, J. Comput. Phys., 125 (1996), pp. 325–337.

[27] R. E. Goldstein, T. R. Powers, and C. H. Wiggins, *Viscous nonlinear dynamics of twist and writhe*, Phys. Rev. Lett., 80 (1998), pp. 5232–5237.

[28] N. S. Cowen, D. M. McQueen, and C. S. Peskin, *Immersed Boundary General Software Package* (IBGSP), available by request from peskin@cims.nyu.edu.

[29] D. M. McQueen, *hrtmvp_readmenu_57.f*, A Three-Dimensional Visualization Program Using Fortran and SGI GL, available by request from mcqueen@cims.nyu.edu.